In Vivo acoustoelectric imaging for high resolution visualization of cardiac electric spatiotemporal dynamics

Alexander Alvarez[1,2], Chet Preston[1], Teodoro Trujillo[1], Cameron Wilhite[3], Alex Burton[1], Sonia Vohnout[2], Russell S. Witte[1,2,3,4,*]

[1]*Deparment of Biomedical Engineering, University of Arizona, 1230 N Cherry Ave, Tucson, AZ 85719, USA*
[2]*Electrosonix, LLC, 435 E 9th St, Tucson, AZ 85705, USA*
[3]*Department of Medical Imaging, University of Arizona, 1230 N Cherry Ave, Tucson, AZ 85719, USA*
[4]*James C Wyant College of Optical Sciences, University of Arizona, 1630 E University Blvd, Tucson, AZ 85719, USA*
** rwitte@optics.arizona.edu*

Abstract: Acoustoelectric Cardiac Imaging (ACI) is a hybrid medical imaging technology that exploits the interaction of an ultrasonic pressure wave and the electrical properties of tissue to map physiologic currents in the heart. In this preliminary study, we used ACI for the first time *in vivo* on a swine model. ACI images demonstrated time-correlation with local cardiac electrograms. Moreover, 2D ACI images exhibited propagation velocities of 0.147 ± 0.092 m/s along the epicardial-endocardial axis and 0.126 ± 0.082 m/s along the apical-basal axis with an SNR of 26 dB. ACI could thus potentially be used to improve diagnosis, staging, and guiding therapy of cardiac arrhythmias.

1. Introduction

Photoacoustic imaging combines light with sound to generate maps with contrast proportional to the absorption of the incident light energy. Although this technique overcomes the optical diffraction limit to image blood vessels and oxygen saturation centimeters deep, it is unable to directly measure bioelectric signals in the body. This study describes a different hybrid imaging modality that uses pressures wave to induce local changes in the electrical properties of tissue, which can be used to produce images of biological currents as they flow through the heart. This hybrid imaging technique not only expands our understanding of the role of electricity in the body, but it also could diagnose and treat diseases with impaired electric function like cardiac arrhythmias.

The heart's mechanical function of pumping oxygenated blood throughout the body relies on coordinated electrical activation of cardiac tissues [1]. When this coordinated electrical activation breaks down – a condition known as an electrical arrhythmia – the heart can no longer pump blood adequately, resulting in severe morbidity and mortality [2]. While standard 12-lead electrocardiography can be used to study the temporal dynamics of arrhythmias and diagnose them as one of several types [3], no known current technologies are capable of noninvasive, high resolution imaging of the 4D (volume + time) spatiotemporal dynamics that drive arrhythmias. Understanding these dynamics could not only help guide appropriate clinical treatment of arrhythmias with currently available drugs, cardioversion, or ablation, but could also help in developing new therapies targeting various mechanisms of disease.

1.1 Limitations with standard cardiac mapping technologies

The gold standard for visualizing spatiotemporal dynamics in the human heart before and after ablation treatment for arrhythmias is electroanatomic mapping (EAM). EAM systems fuse pre-procedural, high resolution anatomical imaging obtained via computed tomography (CT) with

local cardiac electrograms (EGMs) obtained by dragging intracardiac electrodes along various locations in the heart [4,5]. Disadvantages of EAM include invasiveness (an electrophysiology recording catheter must be introduced via the veins into the heart), procedure duration (typically >=2 hours), the necessity for direct contact with convoluted anatomic structures, and difficulty in registering electrical maps to anatomical images leading to errors in accurately locating arrhythmias prior to ablation [6]. Additionally, because EAM relies on contact electrodes, it is unable to capture transmural electrical activation (i.e., the activation across the thickness of the wall of the heart), which can drive arrhythmias and affect the success of ablation procedures.

Recently, novel imaging technologies have been proposed to overcome limitations with conventional EAM. Optical mapping uses voltage- and calcium-sensitive dyes to provide excellent spatial resolution for mapping electrical activation and electromechanical coupling at the cardiac surface due to the physiological dynamics of calcium ion fluxes resulting in electrical activation [7–10]. However, due to the limited penetration depth offered by optical approaches, *in vivo* dynamics would still need to be captured using an invasive catheter-based approach and would not likely be able to visualize electrical dynamics across the wall of the myocardium. Noncontact charge density mapping using a basket array of ultrasound (US) transducers and electrodes promises to solve issues with image registration, time duration, and maintenance of contact to abnormal cardiac anatomy [6]; however, this method still relies on solving an ill-posed inverse problem (i.e., estimating volumetric current densities from potentials measured from an intracardiac electrode array does not have a unique solution). Electromechanical wave imaging is another noninvasive technique that shows promise regarding both resolution and invasiveness by using US speckle tracking to map fast mechanical waves associated with electromechanical coupling; however, this technique is still being tested as a clinical tool and detects only indirect signals related to the underlying electrophysiology [11,12]. In this study, we describe *in vivo* Acoustoelectric Cardiac Imaging (ACI^{TM}), a novel approach to image electrical propagation in the heart, which may overcome limitations with existing methods.

1.2 Acoustoelectric Cardiac Imaging

Acoustoelectric (AE) imaging exploits two physical principles, namely the AE effect and Ohm's law, to map electric currents in the body [13–17]. The AE effect is a modulation of the electrical resistivity ($\rho_0(x,y,z)$) of a material with the application of ultrasonic pressure (ΔP):

$$\Delta\rho = \rho_0 K_I \Delta P \quad \text{(Eq. 1)}$$

where $\Delta\rho(x,y,z)$ is the change in electrical resistivity and $K_I(x,y,z)$ is the acoustoelectric interaction constant in percent change per unit pressure, which has been measured in cardiac tissue to be 0.1%/MPa [18].

In accordance with Ohm's law, when this resistivity change occurs in cardiac tissue where current is flowing, a radiofrequency signal near the ultrasound carrier frequency will be produced and consequently sensed by one or more recording electrodes. This voltage signal (V_{AE}) is proportional to the local current densities in the tissue ($J_I(x,y,z,t_{phys})$) at the focal location of the propagating US wave with pressure amplitude (P_0). The general AE equation is given by:

$$V_{AE}(x_1,y_1,z_1,t_{phys}) = -\iiint [J_L \bullet J_I][K_I \rho_0 P_0 b(x-x_1,y-y_1,z) a(t_{US}-z/c)]dxdydz \quad \text{(Eq. 2)}$$

where $J_L(x,y,z)$ is the lead field (i.e., a vector representing the sensitivity distribution of the recording lead), b is the US beam pattern, and a is the pulse waveform. t_{US} and t_{phys} indicate the US propagation time (in μs) and physiologic time (in ms), respectively. More detailed AE theory and derivations of the general AE equation have been previously described [19–21].

Using this theory to generate ACI movies of electrical signaling, a rapid burst of US pulses from a phased US array is steered to different positions in the heart, and the corresponding V_{AE} is measured by recording electrodes. This approach has been applied to a variety of preparations, such as paced *ex vivo* rabbit and swine hearts [22,23]. Past studies have demonstrated the advantages of AE imaging for high resolution, real-time, volumetric electrical

imaging combined with anatomical information from pulse echo US. Moreover, the noninvasive capability of the technology has been validated by mapping current from a deep brain stimulator through the human skull in a head model [20,24,25], which could be extended to noninvasive transthoracic or transesophageal ACI. In this study, we employed a swine model to demonstrate *in vivo* ACI, which overcomes limitations of existing mapping technologies by accurately characterizing spatiotemporal dynamics of cardiac electrical activation.

2. Methods

2.1 Animal Procedure

All animal procedures and euthanasia were approved and monitored by the Institutional Animal Care and Use Committee. A healthy male swine weighing 25 kilograms was placed under general anesthesia with isoflurane. A thoracotomy was performed with the swine in the supine position to expose the epicardium for electrical recording and ultrasound imaging.

2.2 Signal Acquisition

For ACI, a 10-lead catheter electrode array (ecoLasso catheter; Biosense Webster, Inc; Irvine, CA) was placed on the left ventricle distal to the bifurcation with the diagonal branch (*Fig. 1)* to record low frequency (LF, <10 kHz) bipolar cardiac EGMs and high frequency (HF, >0.2 MHz) AE signals. Signals sensed on the catheter array were passed through a differential amplifier (DA1855; LeCroy Corp; Chestnut Ridge, NY). Signals were then split into low frequency (LF) and high frequency (HF) components in a custom pre-amplifier; HF components of the signal had additional low-pass filtering at 2.5 MHz. LF bipolar EGMs were acquired on a National Instruments DAQ (PXI-6289; National Instruments; Austin, TX) at 20 kHz with 6 V dynamic range; HF AE signals were acquired on a fast acquisition board (PXI-5105; National Instruments; Austin, TX) at 10 MHz with 1 V dynamic range (*Fig. 1*).

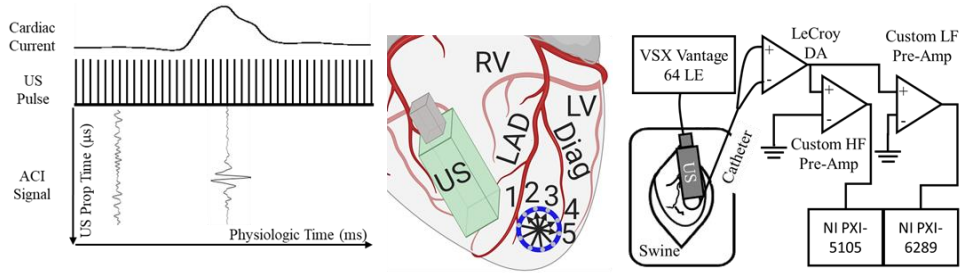

Fig. 1 – Experimental Setup. (*Left*) Timing Diagram of ACI. US Propagation time is converted to depth via multiplication by the medium's speed of sound. (*Middle*) Orientation of bipolar leads and phased array US on the heart in this study (LAD – Left Anterior Descending Artery; Diag – Diagonal Artery; US- Ultrasound; LV – Left Ventricle; RV – Right Ventricle; 1-5 – Bipolar Leads). (*Right*) Connection diagram for *in vivo* ACI hardware setup. LF bipolar EGMs have a gain of 80, whereas HF AE signals have a gain of 4400 (DA = differential amplifier; HF = High Frequency; LF = Low Frequency).

A custom 0.6 MHz 2D US matrix array with 126 (18 x 7) elements (SonicConcepts; Bothell, WA) was acoustically coupled to the epicardium using a waveguide adapter filled with acoustic coupling rubber pressed against the catheter electrodes (*Fig. 1*) [26]. Short US pulses were delivered by the Verasonics commercial US platform (Vantage 64LE; Verasonics, Inc; Kirkland, WA) at 4 kHz pulse repetition frequency (giving a temporal resolution of 250 μs). Ultrasound exposure was maintained at safe levels for diagnostic imaging (i.e., Thermal Index < 1.5 and Mechanical Index < 1.9).

2.3 Signal and Image Processing

Retrospective gating of the EGM and AE signals was performed by using cross-correlation of the depolarization spike of the EGM to align multiple heart beats and facilitate averaging over multiple cardiac cycles.

To form AE M-Mode images (depth vs. time) at a single US beam position, AE signals were bandpass filtered between 0.3 and 0.9 MHz along the US propagation axis and between 10 and 300 Hz along the physiologic time axis. Filtered AE signals were basebanded and converted to the complex envelope using the Hilbert transform for displaying the signed magnitude image, relating to the amplitude and polarity of the local current densities. AE images were also taken at multiple beam positions to produce AE B-Mode movies.

To quantify spatiotemporal dynamics, the peak AE magnitude and 2D position of the peak was determined for each B-Mode frame. 2D spatial vectorgrams were also generated by plotting the peak activation position for each frame. Additionally, propagation velocities were determined by a linear fit over several frames during peak activation. Isochrone maps were generated by determining the peak time delay of the EGM at each pixel in a B-Mode image. Voltage maps were generated by determining the global maximum at each pixel during the cardiac cycle.

3. Results

Fig. 2 depicts a representative AE M-Mode image after averaging over 20 heart beats.

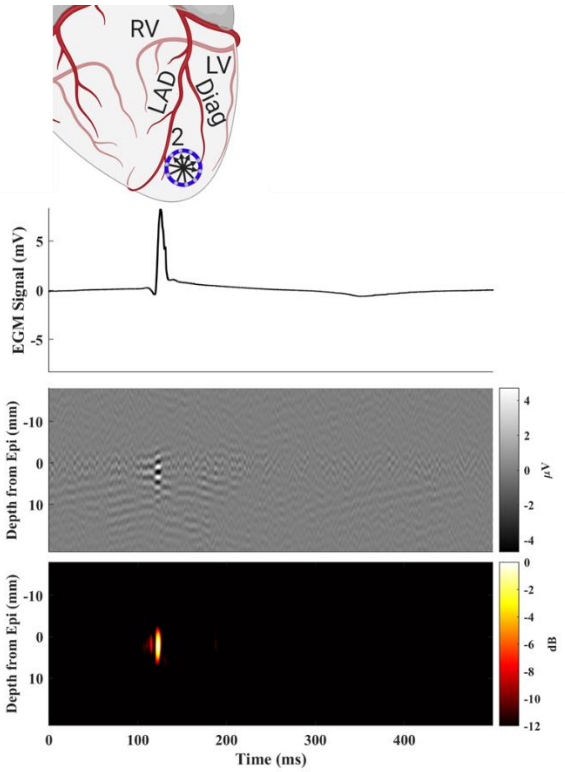

Fig. 2 – *In vivo* ACI M-Mode image from swine LV. *(Top)* LF EGM measured on a single lead as shown in illustration (*Middle*) Filtered AE image after applying bandpass filter (f_b = 0.3-0.9 MHz; f_b = 10-300 Hz) *(Bottom)* Magnitude AE M-Mode image. Epi= epicardium

Fig. 3 displays AE B-Mode images during peak activation averaged over 20 beats. FWHM at peak activation was 6.53 mm and 6.43 mm in the depth and lateral directions, respectively. Signal-to-noise ratio (SNR) at a single frame in these images was 26dB.

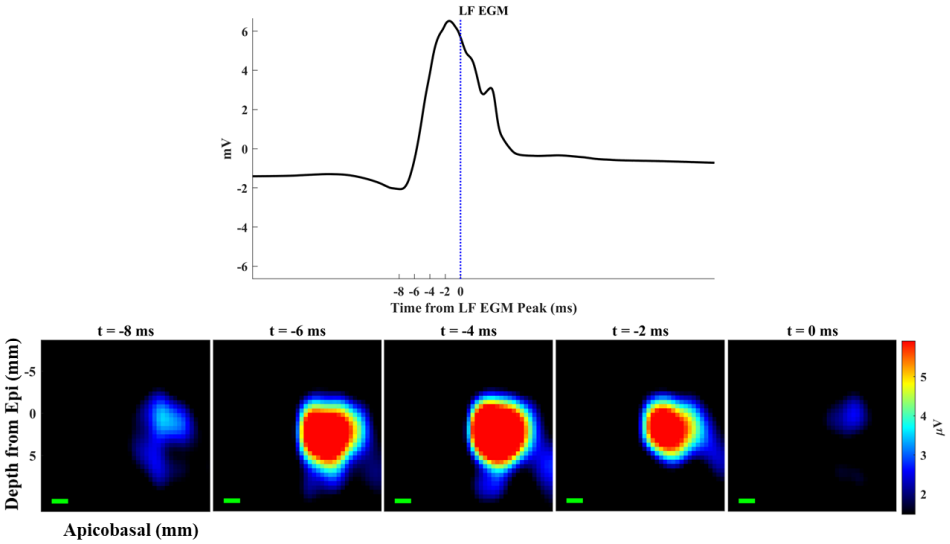

Fig. 3 – *In vivo* AE B-Mode Images in swine LV during peak activation. (*Top*). Bipolar EGM obtained from the lead shown in *Fig. 3*. Vertical line represents peak of the EGM, which is used as the peak time for the remainder of the study. (Bottom). AE B-Mode images on a linear scale demonstrating propagation of signal in the apical and epicardial directions. Green scale bar represents 2 mm in the apical-basal axis.

Fig. 4 compares results for a single heartbeat (SNR=13 dB) to results for an average of 20 beats (SNR=26 dB).

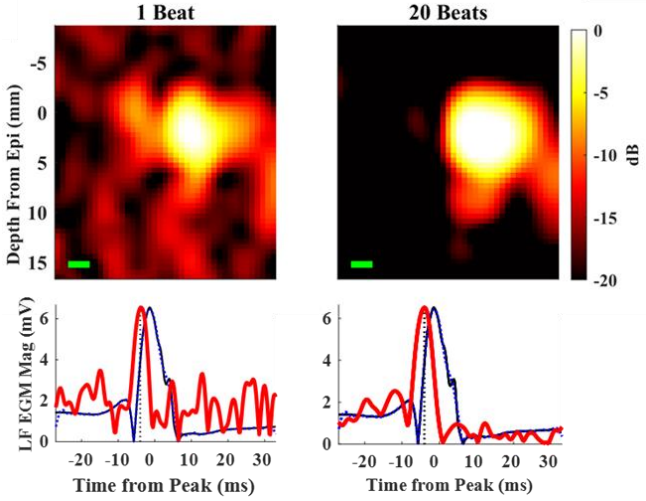

Fig. 4 – Image quality comparing ACI for a single beat vs. an average of 20 cardiac cycles. (*Top Left*) Single beat AE B-Mode 4 ms prior to the peak of the EGM. (*Top Right*) Twenty beat AE B-Mode at the same time point. (*Bottom*) Corresponding normalized slow time AE waveforms at peak signal (red) along with raw and filtered EGM (black/blue). Green scale bar represents 2 mm in the lateral direction (apical-basal axis).

Fig. 5 displays voltage and isochrone maps drawn from an AE B-Mode image. Voltage maps exhibit the maximum voltage at each pixel across all B-Mode frames. Isochrone maps

demonstrate the delay in activation at each pixel, allowing for a visualization of areas that might activate at abnormal times as in arrhythmias. Fig. 5 also presents a vectorgram, indicating spatiotemporal propagation of the signal within an 8 ms window around the peak EGM.

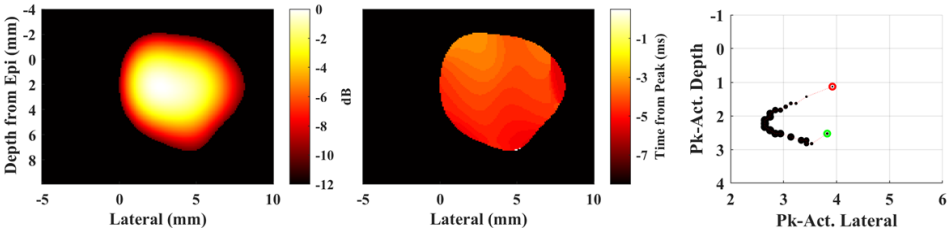

Fig. 5 – Quantifying spatiotemporal dynamics during cardiac activation. (*Left*) AE voltage map displaying the global peak signal at each pixel across all time points. *(Middle*) Isochrone map displaying the delay time to peak of the EGM waveform (above a threshold value of -12 dB), illustrating propagation along the apical-basal and epi-/endocardial axes. *(Right*) Vectorgram displaying the propagation of peak signal in space for each frame starting at 8 ms before the peak of the EGM (green circle) and going to the peak (red circle). The size of the markers are weighted according to the magnitude of the AE signal.

Propagation velocity was calculated from the slope of the best fit line through the peak activation position vs. time plots (Fig. 6). The mean and standard deviation of the propagation velocity over 20 beats was 0.147 ± 0.092 m/s in the depth direction (i.e., epicardial-endocardial axis) and 0.126 ± 0.082 m/s in the lateral direction (i.e., apical-basal axis).

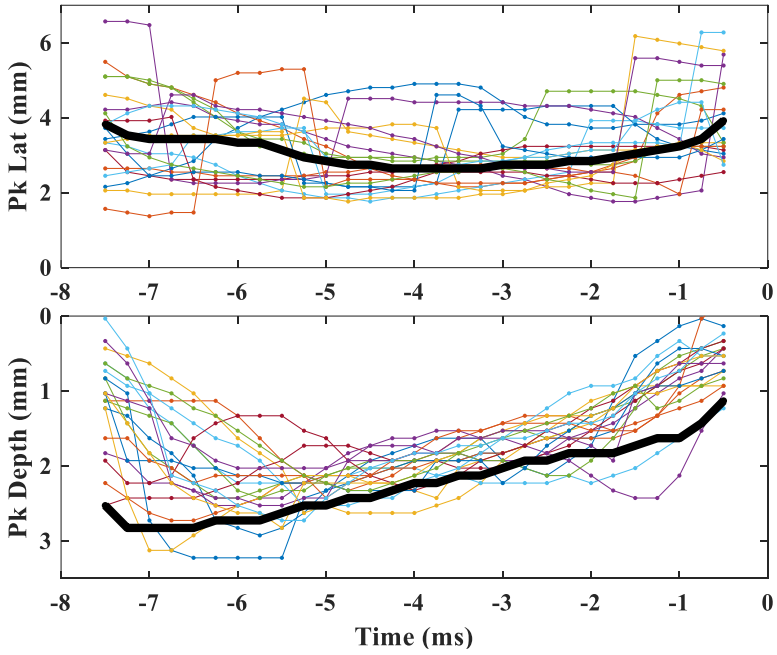

Fig. 6 – Location of peak activation vs. time from the peak LF EGM along the depth and lateral US axes. Whereas each thin dotted line represents propagation for individual beats, the thick black line denotes the average over all beats (n=20). These data were used to calculate propagation velocities.

4. Discussion

This study provided initial results for mapping spatiotemporal dynamics in the swine heart using *in vivo* ACI technology. AE M-Mode images (Fig. 2) demonstrated strong associations in time with LF EGMs measured directly from the epi- or endocardium.

In addition to describing fast temporal dynamics, the AE M-Mode images demonstrate that ACI can capture transmural propagation consistent with depolarization and repolarization of cardiac muscle cells spread across the epi-, myo-, and endocardium. Transmural abnormalities due to scar tissue and electrical dissociation of the endo- and epicardium are considered to be one of several factors that may cause ventricular arrhythmias [27,28]. Because ACI can capture volumetric propagation of signals with high spatial resolution (sub-mm) (Fig.3), it could be a powerful tool in detecting complex arrhythmias that have apical-basal, medial-lateral, and transmural characteristics although this study only demonstrated propagation in 2D. Further improvements to spatial resolution can theoretically be achieved by manipulating the balance between the US probe frequency and sensitivity for detecting the AE signal [22,29].

This study also demonstrated that by using a highly sensitive, low frequency US probe, single beat electrical dynamics can be captured with acceptable SNR (13 dB) (Fig. 4). This ability would allow physicians to tune ACI processing depending on the specific spatiotemporal dynamics they may be looking for. For example, when using ACI to detect arrhythmias that have transient appearances, a single-beat, high sensitivity approach could be used to visualize beat-to-beat variability in real-time and capture the higher frequency components present in many complex arrhythmias [30]. Alternatively, when using ACI to map activation in areas of weaker electrical signaling (e.g., myocardial scar), an approach employing averaging across multiple beats could be employed to ensure signal detection with adequate SNR and/or with higher spatial resolution.

In this study, isochrone and voltage maps were generated from ACI images, which are often used to describe cardiac activation and identify the origin of arrhythmias during ablation therapy similar to what is currently obtained with standard EAM systems [4] (Figs. 5-6). Importantly, unlike in EAM systems, AE voltage maps correspond directly to cardiac current densities rather than EGM potentials. However, the sensitivity distribution of the recording lead (see Eq. 2) also affects the amplitude of the detected signal at each recording site, which leads to inaccuracies. To help correct for lead field effects, it is possible to use multiple recording channel (or leads) for ACI and reconstruct the underlying current densities [21,31].

The isochrone map and vectorgram in Fig. 5 exhibits propagation from the endocardium to the epicardium and from apex to base consistent with normal cardiac electrophysiology [32]. Alterations in isochrones could demonstrate the presence of multiple ectopic arrhythmia sources, which could be captured by ACI's high spatial and temporal resolution.

Finally, the maps in Fig. 7 display complex dynamics as the signal propagates in the heart. The consistency of signal propagation in the depth direction across beats demonstrates the power of this technique to capture endo-epicardial dynamics in real-time. Along with normal physiologic variations in signal propagation, misalignment of the US probe with the apical-basal propagation axis may have led to errors in calculating conduction velocity along this axis. However, by steering the beam in the lateral and elevational directions, volumetric views of the cardiac activation wave would be possible, thereby eliminating this source of variability.

4.1 Conclusion

In summary, this study described *in vivo* ACI in a swine model, combining an ultrasound wave with a sensitive electrical recording system, to map complex electrical activation dynamics in the heart at high spatial (<3 mm) and temporal (<1 ms) resolutions. The noninvasive and high resolution capabilities of ACI potentially overcomes limitations with gold standard approaches to diagnose, stage and treat cardiac arrhythmias.

Funding

Electrosonix, LLC (NIH SBIR R43HL144327), University of Arizona (NIH R43HL144327, T32M132008, T32HL007955, T35HL007479)

Acknowledgments

We thank Dr. Talal Moukabary, MD for feedback in interpreting the swine data, Pier Ingram and the Center for Gamma Ray Imaging for providing the custom 3D printed parts. We would also like to acknowledge Alice McArthur and Debbie Mustacich for their assistance in performing the thoracotomy and documenting the procedures, respectively.

Disclosures

Sonia Vohnout and Russell Witte have a financial interest in ElectroSonix, LLC, which sponsored this study.

References

1. D. M. Bers, "Cardiac excitation-contraction coupling," Nature **415**, 198–205 (2002).
2. M. J. Janse and M. R. Rosen, "History of Arrhythmias," in *Basis and Treatment of Cardiac Arrhythmias*, Handbook of Experimental Pharmacology (Springer, 2006), pp. 1–39.
3. D.-G. Fu, "Cardiac Arrhythmias: Diagnosis, Symptoms, and Treatments," Cell Biochem. Biophys. **73**, 291–296 (2015).
4. D. Bhakta and J. M. Miller, "Principles of Electroanatomic Mapping," Indian Pacing Electrophysiol J **8**, 32–50 (2008).
5. "Advanced Electrophysiologic Mapping Systems," Ont Health Technol Assess Ser **6**, 1–101 (2006).
6. A. Grace, S. Willems, C. Meyer, A. Verma, P. Heck, M. Zhu, X. Shi, D. Chou, L. Dang, C. Scharf, G. Scharf, and G. Beatty, "High-resolution noncontact charge-density mapping of endocardial activation," JCI Insight **4**, (2019).
7. Efimov Igor R., Nikolski Vladimir P., and Salama Guy, "Optical Imaging of the Heart," Circulation Research **95**, 21–33 (2004).
8. I. Hernández-Romero, M. S. Guillem, C. Figuera, F. Atienza, F. Fernández-Avilés, and A. M. Climent, "Optical imaging of voltage and calcium in isolated hearts: Linking spatiotemporal heterogeneities and ventricular fibrillation initiation," PLOS ONE **14**, e0215951 (2019).
9. Hansen Brian J., Li Ning, Helfrich Katelynn M., Abudulwahed Suhaib H., Artiga Esthela J., Joseph Matthew E., Mohler Peter J., Hummel John D., and Fedorov Vadim V., "First In Vivo Use of High-Resolution Near-Infrared Optical Mapping to Assess Atrial Activation During Sinus Rhythm and Atrial Fibrillation in a Large Animal Model," Circulation: Arrhythmia and Electrophysiology **11**, e006870 (2018).
10. P. Lee, J. G. Quintanilla, J. M. Alfonso-Almazán, C. Galán-Arriola, P. Yan, J. Sánchez-González, N. Pérez-Castellano, J. Pérez-Villacastín, B. Ibañez, L. M. Loew, and D. Filgueiras-Rama, "In vivo ratiometric optical mapping enables high-resolution cardiac electrophysiology in pig models," Cardiovasc Res **115**, 1659–1671 (2019).
11. E. E. Konofagou and J. Provost, "Electromechanical wave imaging for noninvasive mapping of the 3D electrical activation sequence in canines and humans in vivo," J Biomech **45**, 856–864 (2012).
12. A. Costet, E. Wan, L. Melki, E. Bunting, J. Grondin, H. Garan, and E. Konofagou, "Non-invasive Characterization of Focal Arrhythmia with Electromechanical Wave Imaging in Vivo," Ultrasound Med Biol **44**, 2241–2249 (2018).
13. R. S. Witte, R. Olafsson, S.-W. Huang, T. L. Hall, and M. O'Donnell, "Acoustic sensor utilizing acoustoelectric effect," United States patent US8427906B2 (April 23, 2013).
14. R. S. Witte, C. INGRAM, Q. Li, and Y. QIN, "ACOUSTOELECTRIC IMAGE-GUIDED THERAPY," U.S. patent 3463070 (n.d.).
15. R. S. Witte, Y. Qin, M. O'donnell, Z. Xu, and C. Ingram, "Handheld Ultrasound Transducer Array for 3d Transcranial and Transthoracic Ultrasound and Acoustoelectric Imaging and Related Modalities," U.S. patent WO/2019/051216 (March 14, 2019).
16. R. S. Witte, R. Olafsson, and M. O'Donnell, "High-resolution mapping of bio-electric fields," United States patent US8057390B2 (November 15, 2011).
17. R. S. Witte, C. PRESTON, Y. QIN, C. INGRAM, and A. BURTON, "Imaging electrical current patterns generated by a medical device," World Intellectual Property Organization patent WO2019051223A1 (March 14, 2019).
18. Q. Li, R. Olafsson, P. Ingram, Z. Wang, and R. Witte, "Measuring the acoustoelectric interaction constant using ultrasound current source density imaging," Phys Med Biol **57**, 5929–5941 (2012).
19. B. Berthon, P.-M. Dansette, M. Tanter, M. Pernot, and J. Provost, "An integrated and highly sensitive ultrafast acoustoelectric imaging system for biomedical applications," Phys. Med. Biol. **62**, 5808–5822 (2017).
20. C. Preston, W. S. Kasoff, and R. S. Witte, "Selective Mapping of Deep Brain Stimulation Lead Currents Using Acoustoelectric Imaging," Ultrasound in Medicine & Biology **44**, 2345–2357 (2018).
21. Renhuan Yang, Xu Li, Aiguo Song, Bin He, and Ruqiang Yan, "A 3-D Reconstruction Solution to Current Density Imaging Based on Acoustoelectric Effect by Deconvolution: A Simulation Study," IEEE Trans. Biomed. Eng. **60**, 1181–1190 (2013).

22. Y. Qin, Q. Li, P. Ingram, C. Barber, Z. Liu, and R. S. Witte, "Ultrasound current source density imaging of the cardiac activation wave using a clinical cardiac catheter," IEEE Trans Biomed Eng **62**, 241–247 (2015).
23. B. Berthon, A. Behaghel, P. Mateo, P.-M. Dansette, H. Favre, N. Ialy-Radio, M. Tanter, M. Pernot, and J. Provost, "Mapping Biological Current Densities With Ultrafast Acoustoelectric Imaging: Application to the Beating Rat Heart," IEEE Trans Med Imaging **38**, 1852–1857 (2019).
24. C. Preston, A. M. Alvarez, A. Barragan, J. Becker, W. S. Kasoff, and R. S. Witte, "High resolution transcranial acoustoelectric imaging of current densities from a directional deep brain stimulator," J. Neural Eng. **17**, 016074 (2020).
25. A. Barragan, C. Preston, A. Alvarez, C. P. Ingram, T. Kanti Bera, and R. S. Witte, "4D Transcranial Acoustoelectric Imaging of Current Densities in a Human Head Phantom," in *2019 IEEE International Ultrasonics Symposium (IUS)* (2019), pp. 2049–2051.
26. Y. Qin, P. Ingram, Z. Xu, M. O'Donnell, and R. S. Witte, "Performance of a transcranial US array designed for 4D acoustoelectric brain imaging in humans," in *2017 IEEE International Ultrasonics Symposium (IUS)* (2017), pp. 1–4.
27. Akar Fadi G. and Rosenbaum David S., "Transmural Electrophysiological Heterogeneities Underlying Arrhythmogenesis in Heart Failure," Circulation Research **93**, 638–645 (2003).
28. C. Antzelevitch and A. Burashnikov, "Overview of Basic Mechanisms of Cardiac Arrhythmia," Card Electrophysiol Clin **3**, 23–45 (2011).
29. A. Alvarez, J. Ferng, C. Preston, C. Ingram, and R. S. Witte, "Effects of Ultrasound Frequency and Beam Pattern on Acoustoelectric Cardiac Imaging," in (2018).
30. J. Morellato, W. Chik, M. A. Barry, J. Lu, A. Thiagalingam, P. Kovoor, and J. Pouliopoulos, "Quantitative spectral assessment of intracardiac electrogram characteristics associated with post infarct fibrosis and ventricular tachycardia," PLoS One **13**, (2018).
31. R. Olafsson, R. S. Witte, S.-W. Huang, and M. O'Donnell, "Ultrasound Current Source Density Imaging," IEEE Trans Biomed Eng **55**, 1840–1848 (2008).
32. R. Mačianskienė, I. Martišienė, A. Navalinskas, R. Vosyliūtė, R. Treinys, B. Vaidelytė, R. Benetis, and J. Jurevičius, "Evaluation of Excitation Propagation in the Rabbit Heart: Optical Mapping and Transmural Microelectrode Recordings," PLOS ONE **10**, e0123050 (2015).